J Eng Math (2007) 59:323–336
DOI 10.1007/s10665-006-9129-z

An analytical model to determine the ultimate load on masonry arch bridges

Amaryllis Audenaert · Herbert Peremans · Genserik Reniers

Received: 11 May 2006 / Accepted: 21 December 2006 / Published online: 10 March 2007

Abstract This paper proposes an analytical elasto–plastic model to describe the behavior of arches. The modeling is carried out using the equations of (i) horizontal equilibrium, (ii) vertical equilibrium and (iii) equilibrium of moments. The latter equations of equilibrium are ordinary differential equations which can easily be solved by adding boundary conditions, imposing restrictions on the horizontal and vertical movement and on the rotation in the abutments of the arch. For masonry arches, including material properties allowing the occurrence of cracks and the subsequent formation of hinges is required. The latter theory has been implemented in a computer program (Matlab), offering numerical simulations. The software was used to illustrate two case-studies, i.e., the assessment of an arch loaded with a vertical point load and one with a horizontal point load.

Keywords Collapse load · Masonry arches · Numerical simulation · Ordinary differential equations

1 Introduction

Masonry arches are one of the oldest types of bridges being still in use. Some have sustained more than one hundred years and are the subject of different and various investigations. Nevertheless researchers agree that they are difficult to analyze and difficult to assess accurately. Woolfenden describes them as "simple in design, complex in behavior" [1].

The earliest and best-preserved stone-arch bridge in the world is the Anji Bridge in China (see Fig. 1). The roadbridge, still in use today, was built during the Sui Dynasty (581–618).

It is a single segmental stone arch, composed of 28 individual arches bonded transversely, 37.02 m in span and rising 7.23 m above the chord line. Narrower in the upper part and wider in the lower, the bridge averages 9 m in width. The main arch ring is 1.03 m thick with protective arch stones on it. Each of its spandrels is perforated by two small arches, 3.8 m and 2.85 m, respectively, in clear span, so that flood water can be drained and the bridge weight is lightened as well. In 1991, the Anji Bridge was named among the

A. Audenaert (✉) · H. Peremans · G. Reniers
Department of Environment, Technology and Technology Management, University Antwerp, Prinsstraat 13, 2000 Antwerpen, Belgium
e-mail: amaryllis.audenaert@ua.ac.be

Fig. 1 The Anji Bridge. (Source : http://www.neville-hadley.com)

world cultural relics of civil engineering, indicating it being equally famous as the Eiffel Tower in Paris, the Panama Canal and the Pyramids in Egypt.

The growing interest in masonry bridges still in use in China, as well as in Europe and elsewhere, has produced substantial attention from the research community, resulting in the development of accurate and efficient methods for their analysis. In this paper we attempt to derive closed-form analytical solutions for the structural stability of an arch bridge with arbitrary shape and subject to both distributed and localized loads.

The rigid-block theory is considered to be the basic model for understanding the fundamental behavior of masonry arches [2–4]. However, this study shows that a more sophisticated approach is required to be able to reproduce the actual collapse mechanism. Rigid-block theory uses too many simplifications and assumptions, the latter frequently deviating excessively from actual conditions. The importance of the rigid-block method resides in its potential to obtain a first insight into the arch behavior.

A more recent research technique uses finite-element analysis. The models range from 1-dimensional [5,6], over 2-dimensional [7–9], up to fully 3-dimensional models [10]. These methods are especially convenient for understanding three-dimensional effects. However, they require a precise knowledge of parameters which are not well-known in practice. For example, they demand a large number of material input-parameters which are difficult to determine for real arches. Moreover, finite-element (FE) programs are often expensive and ask for a certain expertise. Hence, the use of FE software in practical situations is rather limited.

Summarizing, the behavior of arch bridges has been approached in several ways, however until now one "generally accepted" methodology still fails to exist.

2 Collapse modes of arch bridges

According to Boothby [2], an arch bridge can collapse as a result of three possible collapse mechanisms: a shear mechanism (Fig. 2(a)), a hinge-mechanism (Fig. 2(b)) and a combined shear-hinge mechanism (Fig. 2(c)).

His calculations are based on the theory of virtual work. The following conclusions are drawn from this study of possible failure modes for masonry arch bridges:

– Sliding modes of collapse are possible within the range of geometries and material properties of masonry arch bridges.
– Sliding modes may involve three sliding surfaces, or a combination of sliding surfaces and hinges totalling four.

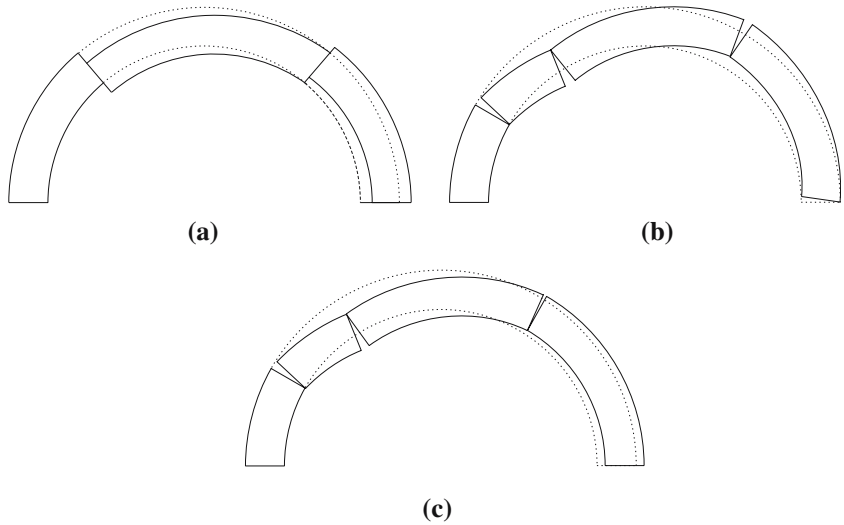

Fig. 2 Collapse modes

Fig. 3 Collapse of the Bridgemill arch bridge. (Source : http://archive.niees.ac.uk/talks/dem/nenad_bicanic.ppt)

- Sliding modes involving three sliding surfaces are more likely to occur in structures with low rise/span ratios and thick arch rings.
- Combined sliding and hinging collapse modes are more likely to occur in structures with low rise/span ratios.
- Hinging collapse modes predominate in structures with high rise/span ratios and narrow arch rings, or structures that are well buttressed.

Experiments show that, due to most arches being well buttressed, the hinge-mechanism can be considered as the most likely collapse mechanism for arches. This mechanism is illustrated by the experiment of Hendry et al. [11], who loaded a real arch bridge until collapse. Fig. 3 illustrates Hendry's experiment. The work presented in this study will concentrate on this mechanism only.

3 Analytical model

First, a basic model guaranteeing stability of arch bridges is developed. Next, material properties are added to derive the formation of hinges.

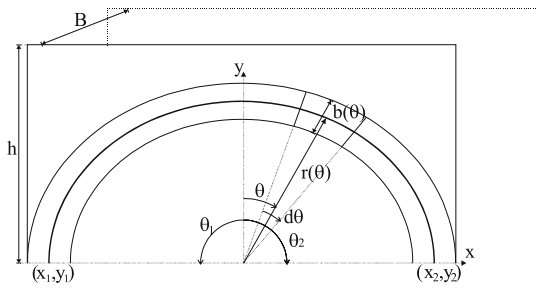

Fig. 4 Arch bridge

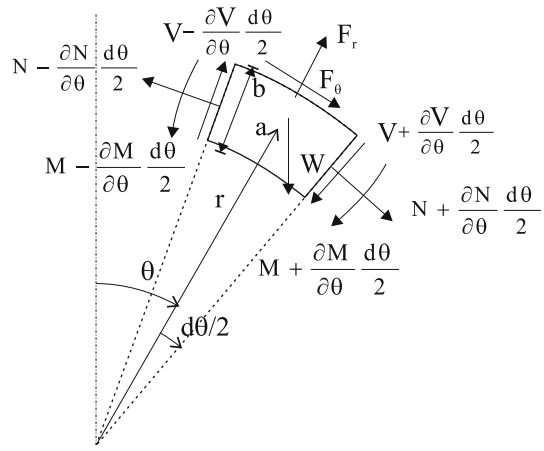

Fig. 5 Equilibrium of an infinitesimal slice of arch

3.1 Equilibrium equations

The starting point for this analysis is the derivation of the three equilibrium equations (i.e., horizontal, vertical and rotational equilibrium) which must be satisfied in every point of an arch bridge. The three types of equilibrium are expressed as continuous equations, as opposed to the discrete approach taken in a finite-element analysis. The geometry of the arch is determined by the angle θ, the radius $r(\theta)$ and the height $b(\theta)$ as shown in Fig. 4.

To derive the differential equilibrium equations, the equilibrium of an infinitesimal piece, angular extent $\mathrm{d}\theta$, of the arch is considered (see Fig. 5).

Figure 5 illustrates the equilibrium of an infinitesimal slice of an arch. The internal forces and moments, i.e., the normal force N (>0 for tension), the shear force V (>0 for a clockwise rotation) and the bending moment M (>0 for compression in the intrados) balance the weight of this segment of arch $W\mathrm{d}\theta$ and the external forces imposed on this slice of arch. The external forces applied to the arch act on the extrados. The latter are summarized, as shown in Fig. 5, by the forces $F_r\mathrm{d}\theta$, acting in the radial direction, and $F_\theta\mathrm{d}\theta$, acting in the tangential direction of this infinitesimal slice. Hence, the three equilibrium equations as they apply to an infinitesimal slice of arch $\mathrm{d}\theta$ can be expressed as:

$$-W(\theta)\cos(\theta)\mathrm{d}\theta - N\mathrm{d}\theta - \frac{\partial V}{\partial\theta}\mathrm{d}\theta + \Sigma F_r\mathrm{d}\theta = 0, \tag{1}$$

$$W(\theta)\sin(\theta)\mathrm{d}\theta - V\mathrm{d}\theta + \frac{\partial N}{\partial\theta}\mathrm{d}\theta + \Sigma F_\theta\mathrm{d}\theta = 0, \tag{2}$$

$$\frac{\partial M}{\partial\theta}\mathrm{d}\theta + N\frac{\partial r}{\partial\theta}\mathrm{d}\theta + Vr\mathrm{d}\theta + M_a(W)\mathrm{d}\theta + M_a(F)\mathrm{d}\theta = 0 \tag{3}$$

with $M_a(W)\mathrm{d}\theta$ and $M_a(F)\mathrm{d}\theta$ denoting the moments of the weight and the external forces with respect to the centreline of the arch given by point a in the infinitesimal slice of arch.

In ref. [12] is shown how the equilibrium equations (1)–(3) result in a set of differential equations. For an arch bridge loaded by (i) its own weight, (ii) a distributed load p, (iii) a concentrated vertical load P and (iv) a concentrated horizontal load H, the differential equations can be written as:

$$-V' - N - \gamma r^2\eta\cos\theta + p_r - P\delta(\theta-\alpha_1)\cos\theta + H\delta(\theta-\alpha_2)\sin\theta = 0, \tag{4}$$

$$N' - V + \gamma r^2 \eta \sin\theta + p_\theta + P\delta(\theta - \alpha_1)\sin\theta + H\delta(\theta - \alpha_2)\cos\theta = 0, \tag{5}$$

$$\begin{aligned} M' + Nr' + Vr + \gamma r^3 \frac{\eta^3}{12}\sin\theta + p_\theta \frac{b}{2} + P\delta(\theta - \alpha_1)|r(\alpha_1)\sin\alpha_1 - r(\theta)\sin\theta| \\ + H\delta(\theta - \alpha_2)|r(\alpha_2)\cos\alpha_2 - r(\theta)\cos\theta| = 0 \end{aligned} \tag{6}$$

with p_r the radial distributed force, p_θ the tangential distributed force, α_1 the position of the vertical point load, α_2 the position of the horizontal point load, γ the specific weight of the arch, $\eta = b/r$ and where a prime denotes the derivative with respect to θ. The load p corresponds to the weight of the infill and eventually to another distributed load as well.

The weight of the infill is actually a distributed load working on the arch barrel. Masonry arch bridges use a quantity of infill above the arch in order to increase the dead-weight on the bridge and prevent tension from occurring in the arch ring as loads move across the bridge. Derivation of this dead-load as a function of the height of the infill h and the specific weight of the infill γ_2 has been worked out by Audenaert et al. [12].

By using the Dirac Distribution $\delta(\theta - \alpha)$ and the unit-step function $u_{\text{step}}(\theta - \alpha)$ definitions, i.e.,

$$\delta(\theta - \alpha) = 0, \quad \theta \neq \alpha \qquad \int_{-\infty}^{+\infty} \delta(\theta - \alpha)\mathrm{d}\theta = 1, \tag{7}$$

$$\begin{aligned} u_{\text{step}}(\theta - \alpha) = 0, &\quad \theta < \alpha \\ 1, &\quad \theta \geq \alpha, \end{aligned} \tag{8}$$

we can solve this set of ordinary linear differential equations analytically for $N(\theta)$, $V(\theta)$ and $M(\theta)$. This results in:

$$\begin{aligned} N(\theta) &= k_1 \sin\theta + k_2 \cos\theta + \sin\theta \int_0^\theta \cos\beta q(\beta)\mathrm{d}\beta - \cos\theta \int_0^\theta \sin\beta q(\beta)\mathrm{d}\beta \\ &\quad - P\sin\theta u_{\text{step}}(\theta - \alpha_1) - H\cos\theta u_{\text{step}}(\theta - \alpha_2), \\ V(\theta) &= k_1 \cos\theta - k_2 \sin\theta + \cos\theta \int_0^\theta \cos\beta q(\beta)\mathrm{d}\beta + \sin\theta \int_0^\theta \sin\beta q(\beta)\mathrm{d}\beta \\ &\quad - P\cos\theta u_{\text{step}}(\theta - \alpha_1) + H\sin\theta u_{\text{step}}(\theta - \alpha_2) + \gamma r^2 \eta \sin\theta + p_\theta, \\ M(\theta) &= k_3 - \int_0^\theta N(\beta) r' d\beta - \int_0^\theta V(\beta) r \mathrm{d}\beta \\ &\quad - \int_0^\theta \left[\gamma r^3 \frac{\eta^3}{12}\sin\beta + p_\theta \frac{b}{2}\right]\mathrm{d}\beta \\ &\quad - P\int_0^\theta \delta(\beta - \alpha_1)|r(\alpha_1)\sin\alpha_1 - r(\beta)\sin\beta|\mathrm{d}\beta \\ &\quad - H\int_0^\theta \delta(\beta - \alpha_2)|r(\alpha_2)\cos\alpha_2 - r(\beta)\cos\beta|\mathrm{d}\beta, \end{aligned} \tag{9}$$

where k_1, k_2 and k_3 are arbitrary constants resulting from solving the differential equations and with

$$q(\theta) = -(\gamma r^2 \eta)' \sin\theta - 2\gamma r^2 \eta \cos\theta - p'_\theta + p_r. \tag{10}$$

Note that this solution offers piecewise continuous expressions for the internal forces and the bending moment.

3.2 Boundary conditions

The general solution of the set of differential equations (9) includes three constants, i.e., k_1, k_2 and k_3. Therefore, to find the unique solution for the internal forces and the bending moment in the arch bridge, we require additional constraints. The boundary conditions introduced below are constraints on the horizontal, vertical and angular deflections of the fixation points of the arch bridge.

The so-called Bresse equations [13, Chapter 6] yield expressions for these deflections, based on the following assumptions:

(i) symmetric cross-section
(ii) load applied in the symmetry plane (the deformed centreline remains in the symmetry plane)
(iii) linear elastic material

Note that condition (ii) is trivially satisfied as we consider a 2D model. Condition iii describes the material behavior in between the hinges. As the arch bridges and external load conditions considered here satisfy all conditions, Bresse's equations express the deflections in every point of the arch bridge in terms of the values for these deflections in one of the boundary points. In particular, Bresse's equations yield the deflections in the right fixed support, given their values in the left fixed support:

$$\varphi_2 = \varphi_1 + \frac{1}{E}\int_{\theta_1}^{\theta_2} \frac{M}{I}\sqrt{r^2 + \left(\frac{\partial r}{\partial \theta}\right)^2}\,\mathrm{d}\theta, \tag{11}$$

$$u_2 = u_1 + (y_2 - y_1)\varphi_1 + \frac{1}{E}\int_{\theta_1}^{\theta_2} \frac{N}{A}\frac{\partial x}{\partial \theta}\mathrm{d}\theta + \frac{1}{E}\int_{\theta_1}^{\theta_2} (y_2 - y)\frac{M}{I}\sqrt{r^2 + \left(\frac{\partial r}{\partial \theta}\right)^2}\,\mathrm{d}\theta, \tag{12}$$

$$v_2 = v_1 - (x_2 - x_1)\varphi_1 + \frac{1}{E}\int_{\theta_1}^{\theta_2} \frac{N}{A}\frac{\partial y}{\partial \theta}\mathrm{d}\theta - \frac{1}{E}\int_{\theta_1}^{\theta_2} (x_2 - x)\frac{M}{I}\sqrt{r^2 + \left(\frac{\partial r}{\partial \theta}\right)^2}\,\mathrm{d}\theta \tag{13}$$

with φ the rotation of the elastic line, u the horizontal deflection, v the vertical deflection, A the area of the cross-section, I = the rotational inertia of the cross-section, E the modulus of elasticity, x the horizontal position coordinate, y the vertical position coordinate, and the subscripts 1 and 2 denoting the left and the right support of the arch bridge, respectively (see Fig. 4).

The sign conventions for the horizontal and vertical deflections u and v are considered the same for both axes x and y and the rotation φ is taken to be positive for clockwise rotations. Both axes are defined as shown in Fig. 4. If the deflections in both supports, i.e., (u_1, v_1, φ_1) and (u_2, v_2, φ_2), are specified, these equations can be used to derive unique values for k_1, k_2 and k_3. The latter can be understood by noting all three functions $N(\theta)$, $V(\theta)$ and $M(\theta)$, as derived above in Eq. 9, are linear functions of the unknown constants k_1, k_2 and k_3. Furthermore, all operators applied to $N(\theta)$ and $M(\theta)$ in Bresse's equations are linear as well. Hence, inserting the expressions derived for $N(\theta)$ and $M(\theta)$ into Bresse's equations will yield a linear set of equations in terms of the unknown constants k_1, k_2 and k_3. Using matrix notation, the equations are expressed as:

$$\overline{E} = A\overline{k} \tag{14}$$

with $\overline{E} = [E_1 \;\; E_2 \;\; E_3]^\tau$, $A = [a_{ij}]$ and $\overline{k} = [k_1 \;\; k_2 \;\; k_3]^\tau$. If matrix A is non-singular, Eq. 14 can be solved to find the unique set of constants k_1, k_2 and k_3. Therefore, this method allows to find the unique solution of the equilibrium equations for a linear elastic arch.

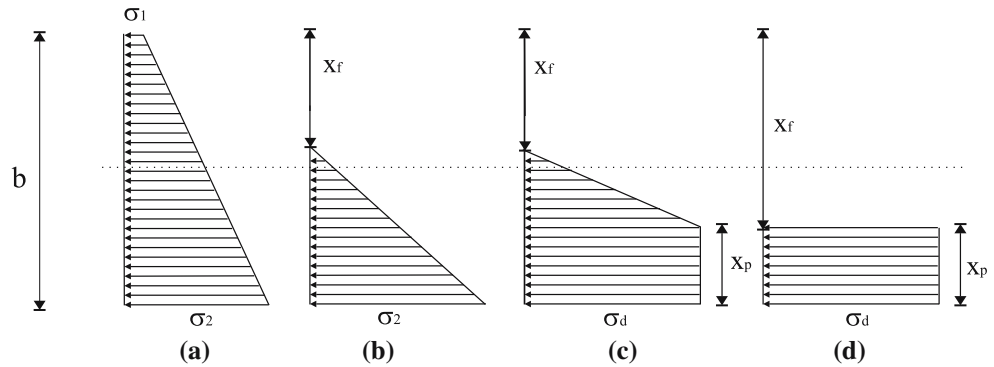

Fig. 6 Evolution of the distribution of stress as the pressure load is increased from (**a**) to (**d**)

3.3 Elastic–plastic material properties

To obtain a satisfying correspondence between theory and experiment, we will have to extend the model presented here by considering the material properties. Lourenço [14, Chapter 2] made a taxonomy of models for masonry into three types, the so-called micro-, meso- and macro-models. In this paper, we use a simplified homogeneous material, which can be classified as a macro-model. In particular, since arch bridges are mostly concrete, masonry or stone constructions, the presence of cracks will have to be taken into account. The following assumptions are made with respect to the behavior of the material:

(i) on reaching the tensile strength σ_t, a crack occurs;
(ii) on reaching the compressive strength σ_d, the material behaves perfectly plastic;
(iii) for $\sigma_d < \sigma < \sigma_t$, the material behaves linearly elastically.

The tensile strength of masonry is accepted to have a minor influence and to be negligible compared with the compressive strength [15]. As a result, we assume $\sigma_t = 0$. In the examples shown below we choose a typical value for the compressive strength, i.e., $\sigma_d = -8\,\text{MPa}$.

Only five stress distributions can occur under these hypotheses: linear-elastic, elasto–fragile, elasto–plastic, elasto–plasto–fragile and plasto–fragile.

Figure 6 shows the evolution of the stress distribution when a cross-section of the arch bridge is subjected to an increasing pressure load, with x_f the height of the crack and x_p the height of the plastic section.

In this last part of Sect. 3.3, we introduce normalized versions of $N(\theta)$ and $M(\theta)$, i.e., the relative normal force $n_d(\theta)$ and the relative moment $m_d(\theta)$.

$$n_d(\theta) = \frac{N(\theta)}{-\sigma_d b(\theta)}, \quad m_d(\theta) = \frac{M(\theta)}{-\sigma_d b^2(\theta)}. \tag{15}$$

Each of the possible stress distributions will mark out a zone in the (n_d, m_d)-plane, containing combinations of the relative normal force $(= n_d)$ and the relative moment $(= m_d)$ in which that specific distribution is possible, as illustrated in Fig. 7.

The border of the elasto–plasto–fragile area corresponds to a plasto–fragile distribution, being consistant with the stress distribution of Fig. 6(d). It reflects those combinations that correspond to the stress distribution of a plastic hinge.

The equation describing this envelope in the compression region is obtained by eliminating x_f and x_p from the expressions for n_d and m_d that apply to the situation shown in Fig. 6(d):

$$|m_d| = \frac{-n_d^2 - n_d}{2}. \tag{16}$$

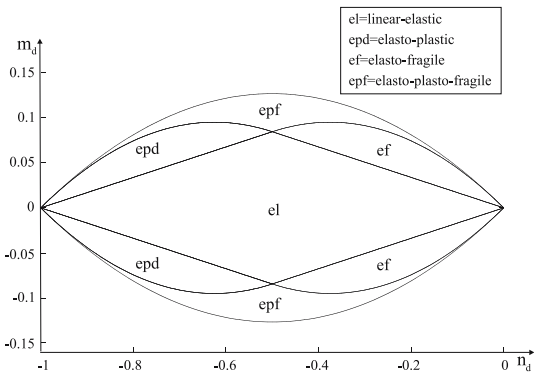

Fig. 7 Envelope of the distribution of stress

3.4 Construction of the model

We will study the failure of masonry arches as a function of a parameter 'x'. This parameter can be any external load. The arch is buttressed at its two ends. Hence, the structure is statically indeterminate to the third degree and will collapse as soon as four hinges have appeared.

Since the results depend linearly upon the studied parameters, we can separate the terms depending upon this parameter x from those that do not, and then rewrite Eq. (14):

$$\overline{C} + x\overline{D} = A(\overline{f} + x\overline{g}). \tag{17}$$

To derive $\overline{f}$ and $\overline{g}$, the matrix equations are inverted:

$$\overline{C} = A\overline{f}, \quad \overline{D} = A\overline{g}. \tag{18}$$

Inserting $\overline{f}$ and $\overline{g}$ in Eq. 9 the internal forces can be expressed in terms of this parameter x making use of the intermediate variables $F_i(\theta)$ and $G_i(\theta)$, $(i = 1, 2, 3)$:

$$N(\theta) = F_1(\theta) + G_1(\theta)x, \quad V(\theta) = F_2(\theta) + G_2(\theta)x, \quad M(\theta) = F_3(\theta) + G_3(\theta)x. \tag{19}$$

To keep the results generalized, we do not further elaborate these expressions at this point. Depending on the nature of the parameter x, the expanded expressions will turn into different forms.

As detecting the occurrence of hinges is performed in the (n_d, m_d)-plane, the internal forces are used to derive expressions for the relative normal force $n_d(\theta)$ and relative moment $m_d(\theta)$.

For notational convenience we first introduce the following terms:

$$\begin{aligned} F_{1d}(\theta) &= \frac{F_1(\theta)}{(-\sigma_d)d}, \qquad G_{1d}(\theta) = \frac{G_1(\theta)}{(-\sigma_d)d}, \\ F_{3d}(\theta) &= \frac{F_3(\theta)}{(-\sigma_d)d^2}, \qquad G_{3d}(\theta) = \frac{G_3(\theta)}{(-\sigma_d)d^2}. \end{aligned} \tag{20}$$

The relative normal force and the relative moment can then be expressed in terms of the parameter x as

$$n_d(\theta) = F_{1d}(\theta) + G_{1d}(\theta)x, \quad m_d(\theta) = F_{3d}(\theta) + G_{3d}(\theta)x. \tag{21}$$

Initially, the arch does not contain any hinges. The first hinge appears for the smallest value of x giving rise to a relative normal force and a relative moment that satisfy Eq. 16. We denote this x-value by $x_{\max 1}$. The angle $\theta = \theta_{\max 1}$ corresponding with this value $x_{\max 1}$ gives the location of this first hinge.

In the presence of one plastic hinge the arch turns into a structure that is statically indeterminate to the second degree. We have kept the standard assumption of constant moments in the hinges from classic

plasticity theory, [16, Chapter 2–3]. In [12] we show that the normal forces in the hinges stay approximately constant as well. An arbitrary rotation can occur in this hinge with a constant bending moment, while the material can be considered elastic in other cross-sections. The equations of equilibrium remain the same for an increasing load, but the boundary conditions are adjusted to represent the changed conditions. With the resulting new equations, the evolution of the relative normal force and the relative moment can be determined under continuously increasing value of x. The equilibrium equations together with the hinge equation in $\theta_{\max 1}$ and the adapted boundary conditions, yield a new matrix equation in terms of Δx. This new variable Δx denotes the increment of x required to generate the next hinge.

The matrix equation can now be rewritten in terms of 'Δx'

$$\overline{C_{\sharp s}} + x\overline{D_{\sharp s}} = A_{\sharp s}(\overline{f_{\sharp s}} + \Delta x\overline{g_{\sharp s}}) \tag{22}$$

with $\sharp$ denoting the number of hinges present in the arch. Using a similar technique as explained previous, the vectors $\overline{f_{\sharp s}}$ and $\overline{g_{\sharp s}}$ can be used to derive expressions for the relative normal force $n_d(\theta)$ and the relative moment $m_d(\theta)$. The smallest value of Δx giving rise to a second pair of relative normal force and relative moment satisfying Eq. 16 is the value $\Delta x_{\max 1}$, i.e., the increment of x corresponding with the second hinge. The value of x that gives rise to two hinges in the arch is then given by $x_{\max 2} = x_{\max 1} + \Delta x_{\max 1}$ and the second hinge is localized by the angle $\theta = \theta_{\max 2}$. The same procedure, i.e., the principle of superposition of effects, is followed for determining the third and fourth hinge. The flow-chart of this algorithm is illustrated in Fig. 8.

The methodology elaborated in this paper (and depicted in Fig. 8) improves the classic approaches along a number of lines. The worked-out examples in the next section serve to illustrate the latter statement.

4 Example 1: Vertical concentrated load

To illustrate the approach described above we determine the hinge location, collapse load, internal forces and deflections for an arch bridge, with circular-shaped centreline and characteristics as given in Table 1.

The boundary conditions are assumed to be

$$\varphi_1 = \varphi_2 = u_1 = u_2 = v_1 = v_2 = 0. \tag{23}$$

A distributed load, i.e., the weight of the infill, and a concentrated load P at $\alpha = 0.75 = 42.97°$, are imposed on the bridge. As indicated in the introduction, the material is assumed to be homogeneous.

The flow-chart of the numerical algorithm used to calculate the results presented in this section is shown in Fig. 8. Note that the formulae used in the calculation of A, $\overline{C}$ and $\overline{D}$ are different depending on the number of hinges present in the arch.

Table 1 Characteristics of an exemplary arch bridge

r[m]	b[m]	$\gamma\left[\frac{\mathrm{N}}{\mathrm{m}^3}\right]$	$\gamma_2\left[\frac{\mathrm{N}}{\mathrm{m}^3}\right]$	h[m]	$E\left[\frac{10^6\mathrm{N}}{\mathrm{m}^2}\right]$	θ_1	θ_2	σ_d[MPa]
1.65	0.5	21,000	21,600	2	5,000	$-\pi/2$	$\pi/2$	-8

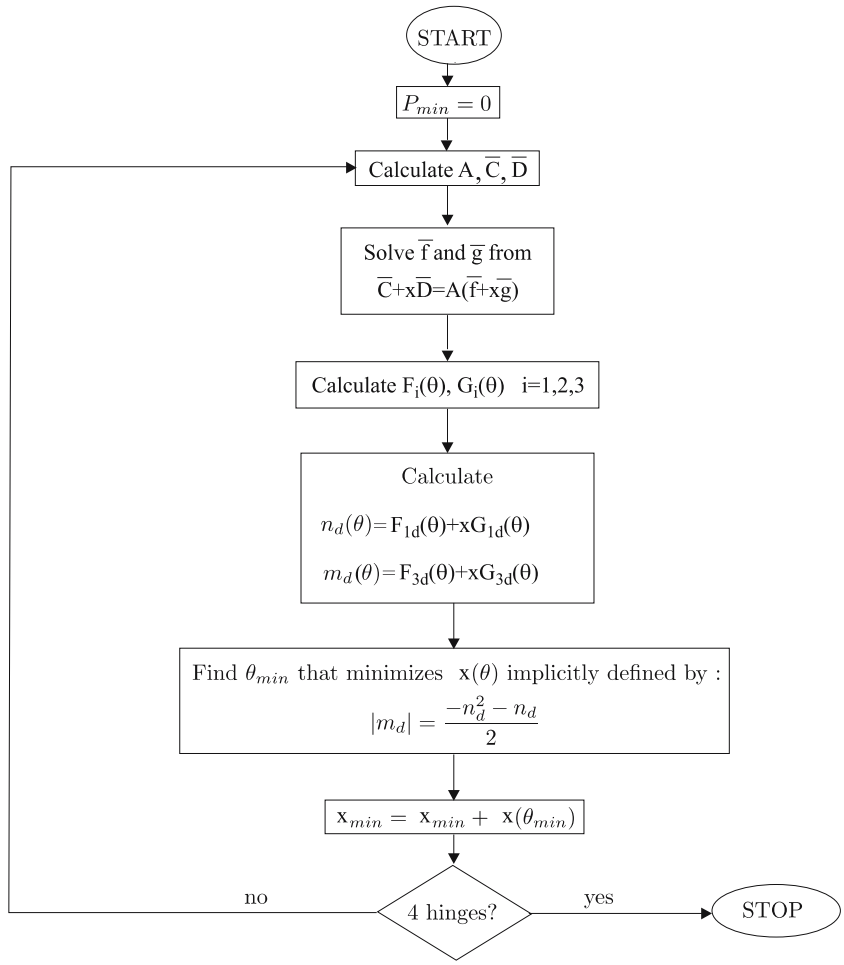

Fig. 8 Flowchart of the numerical algorithm

First, the collapse load and the corresponding hinges are determined. Next, the internal forces and displacements just before collapse are determined. The hinges give rise to:

$$
\begin{aligned}
1st \text{ hinge}: P_{\max 1} &= 40.966 \text{ kN} \\
\theta_{\max 1} &= 0.7461 = 42.75^\circ \\
2nd \text{ hinge}: P_{\max 2} &= 69.75 \text{ kN} \\
\theta_{\max 2} &= -1.5708 = -90^\circ \\
3rd \text{ hinge}: P_{\max 3} &= 94.628 \text{ kN} \\
\theta_{\max 3} &= -0.3971 = -22.75^\circ \\
4th \text{ hinge}: P_{\max 4} &= 137.730 \text{ kN} \\
\theta_{\max 4} &= 1.3483 = 77.25^\circ
\end{aligned}
$$

The collapse load is the sum of all the load terms and is given by $P_{\max} = 1.377 \times 10^5$ N. As can be seen from these results, the first hinge occurs almost exactly under the point where the load is imposed. The second hinge occurs in one of the fixed supports. A third hinge occurs close to (but not exactly in) the other fixation point (see Fig. 9). The formulae to calculate these displacements under a vertical concentrated load are derived in ref. [12]. The location of these hinges as determined with the procedure described above is in

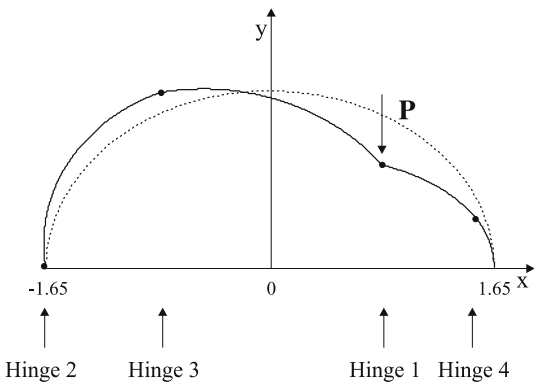

Fig. 9 Displacement centreline under a vertical concentrated load

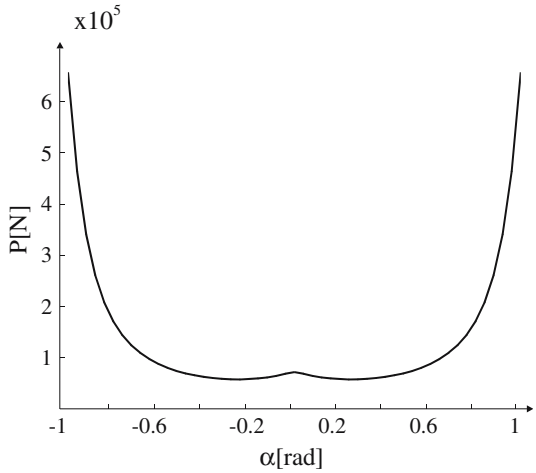

Fig. 10 Collapse load in function of the position of the vertical point load

good agreement with results on failures of arch bridges reported by other authors [2]. Nevertheless, the results reported in this paper indicate that the a priori assumption regarding the occurrence of two hinges in the two support points which is frequently made is only approximately true.

The most important advantage of the analytical model described in this article is easy verification of the sensitivity of the arch behavior to the various parameters used in the model. For instance, the determination of the weakest point of the arch bridge, i.e., the location α corresponding with the smallest collapse load, is of great practical interest. In accordance with the findings of other authors, [17], the calculation procedure described above indicates that $\alpha = 0$ is not the weakest point. In the example this weakest point falls at $\alpha = \pm 0.24 = 13.75°$ as shown in Fig 10. The maximum load possibly imposed on this point is 0.564×10^5 N. This is the vertical collapse load of the arch. The results obtained can also be compared with results obtained by the rigid–plastic approach, using the so-called Ring software [18]. The rigid–plastic model is based on the theory of virtual work, giving rise to upper-bound values for the collapse load. Taking the position of the point load to be the weakest position of the arch, i.e., $\alpha = \pm 0.24 = 13.75°$, we obtain the results presented in Fig. 11. Figure 11 illustrates the numerical values of our collapse loads being smaller than those obtained by the rigid–plastic model, yielding safer calculations. Comparing the hinge locations with one another shows the collapse mechanism being the same for both our *modus operandi* and the rigid-block approach. The collapse load, however, differs for smaller span-height proportions, as shown in Fig. 11. As the effect of the elasticity of the masonry becomes more pronounced for larger cross-sections, the upper bound derived from our model is significantly lower than the one resulting from the rigid-block theory. Nevertheless, a realistic range for the span-height proportion is [11, 21].

5 Example 2: Horizontal concentrated load

We use the same material properties and the same arch bridge as in example 1. However, in this case we impose a horizontal concentrated load at $\alpha = -0.75$. First, the collapse load and the corresponding hinges are determined. Next, the internal forces and displacements just before collapse are determined.

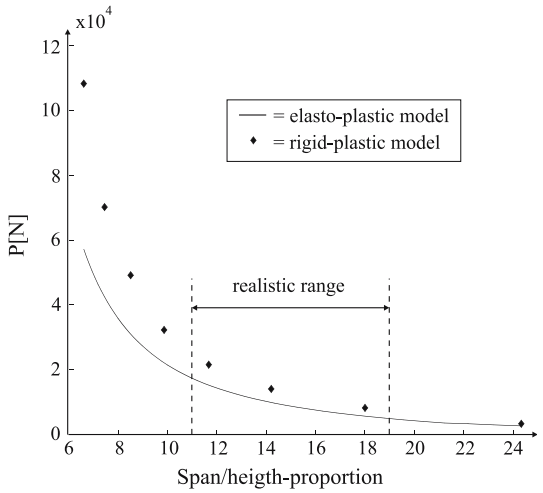

Fig. 11 Validation of the elasto–plastic model against the rigid–plastic model

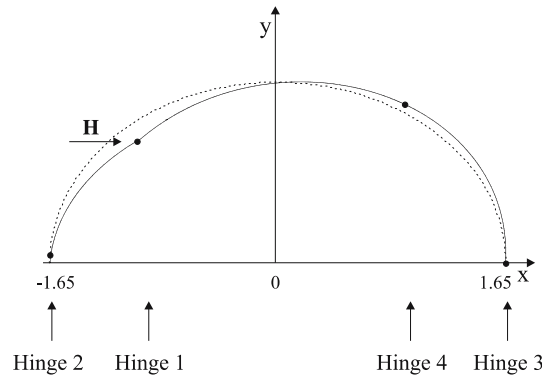

Fig. 12 Displacement centreline under a horizontal concentrated load

$$
\begin{aligned}
1st\ \text{hinge}: H_{\max 1} &= 15.724\,\text{kN} \\
\theta_{\max 1} &= -0.7505\ (-43^\circ), \\
2nd\ \text{hinge}: H_{\max 2} &= 27.218\,\text{kN} \\
\theta_{\max 2} &= -1.5490\ (-88.7512^\circ), \\
3rd\ \text{hinge}: H_{\max 3} &= 29.1869\,\text{kN} \\
\theta_{\max 3} &= 1.5708\ (90^\circ), \\
4th\ \text{hinge}: H_{\max 4} &= 33.1849\,\text{kN} \\
\theta_{\max 4} &= 0.3447\ (19.7499^\circ).
\end{aligned}
$$

The collapse load is the sum of all the load terms and is given by $H_{\max} = 3.3185 \times 10^4$ N. As can be seen from these results, the first hinge occurs almost exactly below the point where the load is imposed. The second hinge occurs close to the fixed support on the side of the load. A third hinge occurs in the other fixation point (see Fig. 12).

Since the internal forces are known at all times, the evolution of the stress distribution in the arch can be traced for increasing load H until the structure collapses. Based on the ratio of n_d and m_d, the type of stress distribution can be determined.

The normal stresses (see Fig. 13), are determined for five different load conditions:

(i) arch loaded by dead load = the weight of the arch and of the infill
(ii) arch loaded by dead load + $H_{\max 1} = 1.5724 \times 10^4$ N,
(iii) arch loaded by dead load + $H_{\max 2} = 2.7218 \times 10^4$ N,
(iv) arch loaded by dead load + $H_{\max 3} = 2.9187 \times 10^4$ N,
(v) arch loaded by dead load + $H_{\max 4} = 3.3185 \times 10^4$ N.

These figures also clearly depict the consecutive hinges coming about.

6 Model limitations

Obviously simplifications are made in the analytical model described in this paper. They can, however, be justified by a desire to minimize complexity and by making the techniques accessible for wider use.

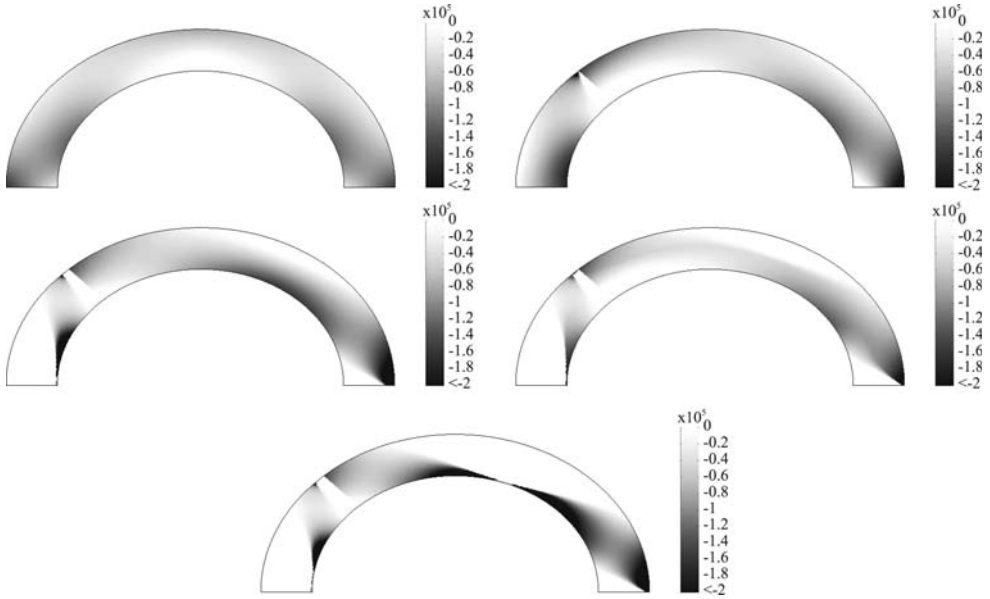

Fig. 13 Evolution of the normal-stress distribution as a function of increasing horizontal load H

Modeling a three-dimensional structure as a two-dimensional construction imposes certain limitations as well. The effects of spandrel walls cannot be included into the model, and behavior transverse to the span cannot be observed.

Due to the method of crack modeling in the arch, cracks are forced to propagate perpendicularly to the arch ring. An improved model could include more crack planes. However, since experiments show that failure of the arch is due to cracks in the mean direction, the other cracks are of minor importance and do not lead to collapse.

The model presented in this paper proves that the elasticity of the arch ring has a big influence on the collapse load. The influence of other material properties, such as Poisson's modulus for the arch barrel and the infill and the elasticity modulus, should be examined. If their requirement can be justified, these properties should be added to the model. Also incorporation of a shear mechanism and a combined shear-hinge mechanism would extend the possibilities of the model.

7 Conclusion and future work

An analytical approach to the collapse analysis of single-span arch bridges has been presented. The model enhances the basic, modern formulation of the theory, presented by Heyman [15]. The main hypotheses in such models are (i) sliding between voussoirs not being allowed to occur, (ii) masonry not being able to resist tension stresses and (iii) the compressive strength of the voussoirs being infinite. The model presented here incorporates material properties such as compressive strength, tensile strength and elasticity modulus of the arch barrel. Another major advantage of our approach is its analytical character, making it suitable for parameter studies.

From a comparison with the rigid-block analysis it is clear that our approach predicts significantly smaller collapse loads than the upper bounds generated by the rigid-block analysis. This is related to the thickness of the arch. As the thickness of the arch increases, the elastic behavior of the material becomes more significant. Hence, the present approach, by taking into account the elastic properties of the material of the arch, will produce more realistic results than a rigid-block analysis possibly could.

This procedure leads to a fast and reasonably accurate assessment of an arch under a wide range of load conditions. Both the locations of the hinges and the collapse load of an arch bridge can be determined. The analytic approach makes it possible to perform parameter studies, e.g., determining the weakest point of an arch bridge. Also, the influence of the other parameters used in the model, such as height of the superstructure, material properties of the arch and/or of the infill, thickness of the ring, etc., can easily be studied by our analytical elastic–plastic model.

To obtain an even better match between the theoretical results and the behavior of the real bridge, more detailed modeling of the bridge is required, e.g., taking into account sliding phenomena as well as the presence of infill and spandrel walls. Also, being a 2-dimensional model, it cannot fully take into account the non-zero width of the bridge. The authors propose building a 3-dimensional finite-element model. Comparing the results from both models, the limits of our model can be investigated more thoroughly.

References

1. Woolfenden PA (1993) Modeling the masonry arch: Improving modern arch bridge assessment using nonlinear finite element software package (MAFEA). Bridge Managment, vol. 2. Thomas Telford, London, pp 254–263
2. Boothby T (1995) Collapse modes of masonry arch bridges. J Brit. Masonry Soc 9(2):62–69
3. Gilbert M, Melbourne C (1994) Rigid-block analysis to masonry arches. Struct Engng 72:356–361
4. Hughes TG, Blackler MJ (1995) A review of the UK masonry assessment methods. Proc Inst Civil Eng 110:373–382
5. Choo BS, Coutie MG, Gong NG (1991) Finite-element analysis of masonry arch bridges using tapered elements. Proc Inst Civil Eng 91:755–770
6. Mollins C, Roca P (1998) Capacity of masonry arches and spatial frames. J Struct Engng 124:653–663
7. Boothby TE, Domalik DE, Dalal VA (1998) Service load response of masonry arch bridges. J Struct Engng 124:17–23
8. Lourenço PB, Rots JG (2000) Failure criterion for masonry suitable for numerical implementation. The Masonry Soc J 18:11–18
9. Ng KH, Fairfield CA, Sibbad A (1999) Finite-element analysis of masonry arch bridges. Proc Inst Civil Eng: Structs Build 134:119–127
10. Fanning PJ, Boothby TE, Roberts BJ (2001) Longitudinal and transverse effects in masonry arch assessment. Construction Build Mater 15:51–60
11. Hendry AW, Davies SR, Royles R (1985) Test on a Stone Masonry Arch at Bridgemill-Girvan. Transport and Road REsearch Lab, Contractors Report 7 United Kingdom
12. Audenaert A, Peremans H, De Wilde WP (2004) Static determination of the internal forces and displacements in arch bridges. The Masonry Soc J 22(1):97–109
13. Timoshenko SP (1983) History of strength of materials. Dover Publications
14. Lourenço PB (1996) Computational strategies for masonry structures. Delft University Press
15. Heyman J (1966) The stone skeleton, Int J Solids Struct 2:249–279
16. Kachanov LM (2004) Fundamentals of the theory of placticity. Dover Publications
17. Brencich A, De Francesco U, Gambarotta L (2001) Elastic no tensil resistant-plastic analysis of masonry arch bridges as an extension of Castigliano's method. The Ninth Canadian masonry symposium at New Brunswich, on 4–6 June 2001
18. RING (2003) The University of Sheffield, www.shef.ac.uk/ring, 2003